Nonlinear Effects in Single-Particle Photothermal Imaging

Claire A. West, †,|| Stephen A. Lee, †,|| Jesse Shooter, † Emily K. Searles, † Harrison J. Goldwyn, † Katherine A. Willets, *,¶ Stephan Link, *,‡,§ and David J. Masiello*, †
†Department of Chemistry, University of Washington, Seattle, Washington 98195, United

States

‡Department of Chemistry, Rice University, Houston, Texas 77005, United States

¶Department of Chemistry, Temple University, Philadelphia, Pennsylvania 19122, United

States

§Department of Electrical and Computer Engineering, Rice University, Houston, Texas

77005, United States

||equal contribution

E-mail: kwillets@temple.edu; slink@rice.edu; masiello@uw.edu

2 Abstract

3

10

Although photothermal imaging was originally designed to detect individual molecules that do not emit or small nanoparticles that do not scatter, the technique is now being applied to image and spectroscopically characterize larger and more sophisticated nanoparticle structures that scatter light strongly. Extending photothermal measurements into this regime, however, requires revisiting fundamental assumptions made in the interpretation of the signal. Herein, we present a theoretical analysis of the wavelength-resolved photothermal image and its extension to the large particle scattering regime where we find the photothermal signal to inherit a nonlinear dependence

upon pump intensity together with a contraction of the full width at half maximum of its point spread function. We further analyze theoretically the extent to which photothermal spectra can be interpreted as an absorption spectrum measure, with deviations between the two becoming more prominent with increasing pump intensities. Companion experiments on individual 10, 20, and 100 nm radius gold nanoparticles evidence the predicted nonlinear pump power dependence and image contraction, verifying the theory and demonstrating new aspects of photothermal imaging relevant to a broader class of targets.

Introduction

The challenge of optically detecting individual nano-objects that do not scatter or emit light has inspired the development of a variety of detection techniques capable of distinguishing absorption independently from scattering and emission. 1,2 One such approach that has been applied to measure small, non-scattering dielectric and metallic nanoparticles is photothermal imaging. 3-5 This technique relies on the nanoparticle's resonant absorption of light and associated heat power dissipated into a locally modified temperature and refractive index gradient in the surrounding medium—a so-called "thermal lens"—through which the nanoparticle can be detected. The thermal lens is large, so that its scattering of a second, ideally non-resonant, (probe) beam of light produces the photothermal signal when interfered against itself. Lock-in detection to the modulated amplitude of the pump provides a further means to isolate this interference component from the total signal that reaches the detector.

More recently, however, photothermal techniques have been used to detect individual plasmonic metal nanoparticles and nanoparticle assemblies that are large enough to both absorb and scatter light. ⁶⁻¹⁰ By varying the pump wavelength, photothermal absorption spectra have also been measured from the same nanostructures, independent from scattering. ¹¹⁻¹⁴ In this size regime, fundamental assumptions made in the original photothermal

models are not always valid and interpreting the photothermal signal has been found to require careful reconsideration. ^{6,15} In parallel, other interferometric techniques similar to photothermal imaging have been pioneered to study larger, scattering nanoparticle systems. Two such approaches, coherent brightfield microscopy (COBRI) and interferometric scattering microscopy (iSCAT) are closely related to photothermal imaging, but do not involve optically heating the target specimen. ^{16,17} In both cases, the signal originates from the interference between the field scattered by the (room temperature) target and a reference field without need for lock-in detection. Often, the reference field is either the transmitted (COBRI) or reflected (iSCAT) probe beam.

While the interferometric nature of COBRI and iSCAT allows for small, weakly scattering particles to be detected, they are fundamentally measures of extinction and therefore do not separate absorption from scattering in particles large enough to appreciably scatter. In contrast, photothermal measurements isolate the pure absorption response. However, interpretation of the photothermal signal produced by nano-objects large enough to scatter requires careful consideration of the additional effects of target scattering beyond those induced by the thermal lens. 5,18-20 Here we incorporate these effects within a dipole model that includes effects of the heat diffusion dynamics, co-focusing of pump and probe beams, pump modulation, and lock-in detection. Importantly, for large nanoparticles we find that a new scattering-induced component influences the absorption character of the photothermal signal, and this scattering contribution grows nonlinearly with pump power at fixed pump and probe wavelengths.

As a companion to the presented photothermal scattering model, we acquire experimental data from individual spherical gold nanoparticles ranging in size from 10 to 100 nm in radius.

Despite the small thermo-optic responses of the target and medium, we observe a nonlinearity in the photothermal signal with increasing pump power for the larger nanoparticles. Based on the model presented, we trace the origins of this nonlinearity to a scattering contribution to the photothermal signal that has been disregarded in the small particle limit but that

becomes important for larger scatterers at higher pump power or smaller pump beam waist.

Below, we present the generalized photothermal model and analyze the signal in the
limit of both small and large nanoparticle targets. Further analysis and exploration is
made through a numerical investigation of the pump-wavelength-resolved photothermal
spectra and pump-power-dependent photothermal images of plasmonic nanoparticle absorbers/scatterers of varying size. Finally, we present experimental measurements of the
photothermal signal acquired from individual gold nanoparticles as a function of pump power
and interpret these data from the perspective of the model presented.

72 Generalized Photothermal Signal

In photothermal imaging, the signal that reaches the detector is produced from the superposition of a transmitted/reflected probe beam (or reference field) \mathbf{E}_{pr} and a scattered probe beam \mathbf{E}_{sca} . The pump field that heats the system \mathbf{E}_{pu} is removed by spectral filtering before reaching the detector, resulting in the signal

$$I_{\text{det}}(t) = \frac{cn_b}{8\pi} \left[|\mathbf{E}_{\text{pr}}(t)|^2 + 2\text{Re}[\mathbf{E}_{\text{pr}}(t) \cdot \mathbf{E}_{\text{sca}}^*(t)] + |\mathbf{E}_{\text{sca}}(t)|^2 \right]$$
(1)

at the probe wavelength λ , where c is the speed of light in vacuum, and n_b is the room temperature refractive index of the background medium. Due to the scattering inefficiency of small nano-objects, the $|\mathbf{E}_{\text{sca}}|^2$ term can be safely neglected relative to the term linear in \mathbf{E}_{sca} for the vast majority of targets that have been investigated in the literature using photothermal techniques. However, for larger targets, such as for plasmonic nanoparticle antennas, the $|\mathbf{E}_{\text{sca}}|^2$ term can become important and should be retained. In this section we expose the effects of \mathbf{E}_{sca} upon the photothermal signal.

Lock-in detection is implemented in photothermal measurements to retrieve the interference signal at the modulation frequency. Here we will consider amplitude modulation of the pump beam at frequency Ω , a rate that is typically on the order of kHz to MHz. The outcome of the measurement depends on the order of magnitude of Ω , ²¹ and this work specializes to the low modulation regime where $\Omega = 100$ kHz. The detector locks in only to those signals which vary in-phase and in quadrature with this oscillation frequency, thus projecting out the contribution from the transmitted (and unmodulated) probe producing the following magnitude $|\Phi|$ and phase Ψ^{19}

$$|\Phi| = \sqrt{\Phi_{\sin}^2 + \Phi_{\cos}^2} \qquad \Psi = \tan^{-1} \left[\frac{\Phi_{\sin}}{\Phi_{\cos}} \right]$$
 (2)

of the complex signal $\Phi = |\Phi|e^{i\Psi}$, which are determined from

$$\Phi_{\text{cos}} = \frac{\Omega}{2\pi} \int_{0}^{2\pi/\Omega} \frac{I_{\text{det}}(t)}{(cn_{b}/8\pi)|\mathbf{E}_{\text{pr}}|^{2}} \begin{Bmatrix} \sin \Omega t \\ \cos \Omega t \end{Bmatrix} dt$$

$$= \frac{\Omega}{2\pi} \int_{0}^{2\pi/\Omega} \frac{2\text{Re}[\mathbf{E}_{\text{pr}}(t) \cdot \mathbf{E}_{\text{sca}}^{*}(t)] + |\mathbf{E}_{\text{sca}}(t)|^{2}}{|\mathbf{E}_{\text{pr}}|^{2}} \begin{Bmatrix} \sin \Omega t \\ \cos \Omega t \end{Bmatrix} dt. \tag{3}$$

Lock-in detection, therefore, isolates a part of Φ that stems from the interference between transmitted/reflected and scattered probe $(\Phi_{\rm int} \propto {\rm Re}[\mathbf{E}_{\rm pr} \cdot \mathbf{E}_{\rm sca}^*])$, but also selects a contribution originating from the photothermally-induced probe scattering $(\Phi_{\rm sca} \propto |\mathbf{E}_{\rm sca}|^2)$. $\Phi_{\rm int}\{_{\rm cos}^{\rm sin}\}$ is well understood to result in a photothermal signal that is a measure of absorption. However, the additional effects that $\Phi_{\rm sca}\{_{\rm cos}^{\rm sin}\}$ imparts upon the signal are less well understood as they would only arise for targets large enough to scatter the probe.

The heating and probe lasers used in our analysis are modeled as focused Gaussian beams. The electric field of a Gaussian beam, which propagates in the +z direction, is polarized in the x direction, and is focused at the position z_f is well approximated by

$$\mathbf{E}_{G}(\mathbf{x},t) = E_{0}\hat{\mathbf{x}}\frac{w_{0}}{w(z)}e^{-(x^{2}+y^{2})/w(z)^{2}}e^{ik(z-z_{f})}e^{ik(x^{2}+y^{2})/2R(z)}e^{-i\psi(z)}e^{-i\omega t},$$
(4)

where w_0 is the beam waist at the focus, $w(z) = w_0 \sqrt{1 + (z - z_f)^2/z_R^2}$ is the beam radius, $R(z) = (z - z_f)[1 + z_R^2/(z - z_f)^2]$ is the radius of curvature of the beam, $\psi(z) = \tan^{-1}[(z - z_f)/z_R]$ is the Gouy phase, and $z_R = \pi w_0^2 n_b/\lambda$ is the Rayleigh length at frequency $\omega = 2\pi n_b c/\lambda.$

The reference field is determined by the transmitted field of the incident probe beam evaluated at the detector position \mathbf{x}_{d} , which is assumed to be located on the optical axis in the far field. The detected transmitted/reflected probe field is related to the incident probe field via scaling by the Fresnel transmission/reflection coefficients specific to the system and collection geometry. In the following, we set the transmission coefficient to unity. $\mathbf{E}_{sca}(\mathbf{x},t) = \mathbf{G}(\mathbf{x},\mathbf{x}_{np}) \cdot \alpha_{pt}(t)\mathbf{E}_{G}(\mathbf{x}_{np},t)$ represents the scattered field of a dipole, where $\mathbf{G}(\mathbf{x},\mathbf{x}_{np}) = [k^2\mathbf{I} + \nabla\nabla] \exp(ik|\mathbf{x} - \mathbf{x}_{np}|)/|\mathbf{x} - \mathbf{x}_{np}|$ is the dipole relay tensor, \mathbf{x}_{np} is the position of the nanoparticle target, assumed to be at the origin $(\mathbf{x}_{np} = \mathbf{0})$, and $\alpha_{pt}(t)$ is the time-dependent photothermal polarizability of the nanoparticle's induced dipole. When evaluated at the detector and nanoparticle, the Gaussian beam is well approximated by

$$\mathbf{E}_{G}(\mathbf{x}_{d}, t) \underset{z \gg z_{f}}{\sim} \frac{E_{0}\hat{\mathbf{x}}}{iz/z_{R}} e^{ik(z-z_{f})} e^{-i\omega t}$$

$$\mathbf{E}_{G}(\mathbf{x}_{np} = \mathbf{0}, t) = \frac{E_{0}\hat{\mathbf{x}}}{\sqrt{1 + (-z_{f}/z_{R})^{2}}} e^{-ikz_{f}} e^{-i\tan^{-1}(-z_{f}/z_{R})} e^{-i\omega t},$$
(5)

where $w(z) \approx w_0(z/z_R)$ and $e^{-i\psi(z)} \approx -i$ at the detector $(z \to +\infty)$. Using these limiting forms, the probe and scattered fields become

$$\mathbf{E}_{\mathrm{pr}}(\mathbf{x}_{\mathrm{d}},t) \underset{z\gg z_{\mathrm{pr}}}{\sim} \frac{E_{0}\hat{\mathbf{x}}}{iz/z_{R}} e^{ik(z-z_{\mathrm{pr}})} e^{-i\omega t}$$

$$\mathbf{E}_{\mathrm{sca}}(\mathbf{x}_{\mathrm{d}},t) \underset{z\gg z_{\mathrm{pr}}}{\sim} \frac{k^{2}(\mathbf{1}-\hat{\mathbf{n}}\hat{\mathbf{n}})e^{ikr}}{r} \cdot \alpha_{\mathrm{pt}}(t) \frac{E_{0}\hat{\mathbf{x}}}{\sqrt{1+(-z_{\mathrm{pr}}/z_{R})^{2}}} e^{-ikz_{\mathrm{pr}}} e^{-i\tan^{-1}(-z_{\mathrm{pr}}/z_{R})} e^{-i\omega t}$$

$$(6)$$

at the detector position $\mathbf{x}_{\rm d}=r\hat{\mathbf{n}}$, where $\mathbf{G}(\mathbf{x},\mathbf{x}')$ takes on its far-field form and where $k=2\pi n_b/\lambda$ and $z_{\rm pr}$ denote the wavenumber and focal point of the probe.

As a result, the interference and scattering contributions to the lock-in integral in Eq. 3

are

$$\Phi_{\text{int}}(t) = \frac{2\text{Re}[\mathbf{E}_{\text{pr}}(t) \cdot \mathbf{E}_{\text{sca}}^{*}(t)]}{|\mathbf{E}_{\text{pr}}|^{2}} = \frac{4}{w_{0}^{2}\sqrt{1 + (z_{\text{pr}}/z_{R})^{2}}} k \text{Im} \left[\alpha_{\text{pt}}(t)^{*}e^{i \tan^{-1}(-z_{\text{pr}}/z_{R})}\right]
\Phi_{\text{sca}}(t) = \frac{|\mathbf{E}_{\text{sca}}(t)|^{2}}{|\mathbf{E}_{\text{pr}}|^{2}} = \frac{1}{z_{R}^{2} + z_{\text{pr}}^{2}} k^{4} |\alpha_{\text{pt}}(t)|^{2}$$
(7)

evaluated on the optical axis ($\theta = \phi = 0^{\circ}$) with $z \sim r$ at the detector. Already, a superficial analogy between these expressions and the extinction ($\sigma_{\rm ext}(\omega) = 4\pi(\omega/c) {\rm Im}[\alpha(\omega)] \to \sigma_{\rm abs}(\omega)$ in the small particle limit) and scattering ($\sigma_{\rm sca}(\omega) = (8\pi/3)(\omega/c)^4 |\alpha(\omega)|^2$) cross sections of a dipole of polarizability α are evident. However, there are important differences that will be discussed below, most notably the fact that Eq. 7 involves the photothermal polarizability $\alpha_{\rm pt}$ explicitly and not the dipole Mie polarizability α . $\alpha_{\rm pt}$ is a function of the absorption cross section $\sigma_{\rm abs}$ and pump intensity $I_{\rm pu}$, both of which are functions of the pump wavelength $\lambda_{\rm pu}$ and not the probe wavelength λ . Up to this point, we have made no assumptions about the type of material giving rise to $\alpha_{\rm pt}$. Therefore Eq. (7) is the generalized expression within the dipole limit for the interference and scattering contributions to the lock-in integral in Eq. 3.

Polarizability Model

From these primitive functions, lock-in detection extracts the measured signal, but first a 104 model of the photothermal polarizabilty $\alpha_{\rm pt}$ must be adopted. We choose $\alpha_{\rm pt}$ to describe the 105 time- and temperature-dependent response of a spherical target embedded in a background 106 medium of constant refractive index. Note that while a substrate is not included in this 107 model, it may be accounted for by using a more sophisticated polarizability model or through 108 numerical simulation. Specifically, we focus on two extreme cases: (1) the photothermal 109 signal in the thermal lens limit where the polarizability accounts only for the scattering from 110 the heated medium surrounding a point absorber, and (2) a generalized core-shell model 111 where the core now includes the radiation-damped response of a nanoparticle scatterer in 112

addition to the scattering induced by its thermal lens shell.

In either case, since the thermo-optic coefficients of the target and medium are small $(dn/dT \sim 10^{-4} \text{ K}^{-1})$, the temperature dependence of the target may be approximated at first order by

$$\alpha_{\rm pt}(t) \approx \alpha_{\rm pt}(T_0) + \frac{d\alpha_{\rm pt}}{dn} \frac{dn}{dT} \Big|_{T_0} (T(\mathbf{x}, t) - T_0),$$
 (8)

where $\alpha_{\rm pt}(T_0) \equiv \alpha(T_0)$ is the room temperature Mie polarizability. See the Supporting In-114 formation for a discussion on the appropriateness of this approximation. We calculate the 115 temperature $T(\mathbf{x},t)$ from the time-dependent heat diffusion equation assuming the modu-116 lated heat power $P_{\rm abs}(t) = \sigma_{\rm abs}(\lambda_{\rm pu})I_{\rm pu}(1+\cos\Omega t)/2$ absorbed by a point absorber in the 117 small particle limit or a spherical absorber in the large particle limit. Given that $T(\mathbf{x},t)$ is 118 a function of $I_{\rm pu}$, the photothermal polarizability $\alpha_{\rm pt} \equiv \alpha_{\rm pt}(I_{\rm pu})$ is therefore a nonlinear re-119 sponse function, as it depends upon the pump intensity $I_{\rm pu}$ (or pump power $P_{\rm pu}=I_{\rm pu}\pi w_{\rm pu}^2/2$, 120 where w_{pu} is the pump waist evaluated at the nanoparticle) through its temperature depen-121 dence. It also encodes the geometry-specific resonant responses of the target through the 122 absorption cross section $\sigma_{abs}(\lambda_{pu})$, which itself is a function of the linear Mie polarizability $\alpha(\lambda_{pu})$ of the target's induced dipole moment at room temperature T_0 .

125 Small Particle Limit

Small $(ka \ll 1)$ metal nanoparticles do not scatter. Instead they absorb light and dissipate optical heat power into a temperature rise of the surrounding medium. In this limit, it is appropriate to model the optical response as a thermal lens, or a large sphere of heated background with volume $V_{\rm th}$ with Clausius-Mossotti polarizability

$$\alpha_{\rm pt}(t) = \frac{3V_{\rm th}}{4\pi} \varepsilon_b \frac{\varepsilon(T) - \varepsilon_b}{\varepsilon(T) + 2\varepsilon_b},\tag{9}$$

where $\varepsilon(T(t))$ is the temperature-dependant dielectric function of the background medium shell and ε_b is the room-temperature dielectric function of the remaining bulk. Since $\varepsilon = n^2$ and $\varepsilon(T=T_0)=\varepsilon_b=n_b^2$, $d\alpha/dn|_{T=T_0}=(V_{\rm th}/2\pi)n_b$, and $\alpha_{\rm pt}(T_0)=0$. Thus,

$$\alpha_{\rm pt}(t) = \frac{V_{\rm th}}{2\pi} n_b \frac{dn_b}{dT} \bar{T}(t) \tag{10}$$

to lowest order, where the average temperature $\bar{T}(t)$ is defined by integrating the temperature rise $T(\mathbf{x}, t) - T_0$ over the volume $V_{\rm th} = (4/3)\pi r_{\rm th}^3$, where $r_{\rm th} = \sqrt{2\kappa/c_p\Omega}$ is the thermal radius with background medium thermal conductivity κ and specific heat capacity c_p . Specifically,

$$\bar{T}(t) = \frac{1}{V_{\rm th}} \int_0^{r_{\rm th}} \frac{\sigma_{\rm abs}(\lambda_{\rm pu}) I_{\rm pu}}{8\pi\kappa r} \left[1 + e^{-r/r_{\rm th}} \cos\left(\Omega t - r/r_{\rm th}\right) \right] 4\pi r^2 dr
= \frac{\sigma_{\rm abs}(\lambda_{\rm pu}) I_{\rm pu} r_{\rm th}^2}{4e\kappa V_{\rm th}} \left[e - \cos(1 - \Omega t) + e \sin(\Omega t) + 2\sin(1 - \Omega t) \right].$$
(11)

Note that since \bar{T} depends upon the pump intensity $I_{\rm pu}$ and absorption cross section $\sigma_{\rm abs}$, the photothermal polarizability $\alpha_{\rm pt} \equiv \alpha_{\rm pt}(\sigma_{\rm abs}, I_{\rm pu})$ is a nonlinear response function that also, in principle, encodes the resonant excitations of the absorbing target through $\sigma_{\rm abs}$.

Using Eq. 7, and neglecting Φ_{sca} , the lock-in integral in Eq. 3 becomes

$$\Phi_{\text{int}\left\{\substack{\sin \\ \cos s}\right\}} = \frac{4k}{w_0^2 \sqrt{1 + (z_{\text{pr}}/z_R)^2}} \text{Im} \left[e^{i \tan^{-1}(-z_{\text{pr}}/z_R)} \frac{\Omega}{2\pi} \int_0^{2\pi/\Omega} \frac{d\alpha_{\text{pt}}^*}{dT} \Big|_{T_0} \bar{T}(t) \begin{Bmatrix} \sin \Omega t \\ \cos \Omega t \end{Bmatrix} dt \right]$$

$$= -\frac{4\sigma_{\text{abs}}(\lambda_{\text{pu}})}{\kappa \lambda} \cdot \frac{P_{\text{pu}}}{\pi w_{\text{pu}}^2} \cdot n_b^2 \frac{dn_b}{dT} \cdot \frac{r_{\text{th}}^2}{w_0^2} \cdot \frac{z_{\text{pr}}/z_R}{1 + (z_{\text{pr}}/z_R)^2} \begin{Bmatrix} \mathcal{I}_1 \\ \mathcal{I}_2 \end{Bmatrix}$$
(13)

when evaluated along the optical axis, where $\sin(\tan^{-1}(x)) = x/\sqrt{1+x^2}$, $\mathcal{I}_1 = (e-2\cos(1)-\sin(1))/4e$, $\mathcal{I}_2 = (2\sin(1)-\cos(1))/4e$, and $\lambda = 2\pi n_b/k$ is the probe wavelength. This result, which is limited to the thermal lens approximation, is consistent with other photothermal models from the literature, such as, e.g., Ref., ¹⁹ and is identical to what was derived in Ref. ²² after inserting the explicit Gaussian beam form in Eq. 4 into the equations presented therein.

135 Large Particle Limit

Outside of the small particle limit, larger nanoparticle targets scatter electromagnetic radiation when $ka \gtrsim 1$. Thus it is to be expected that their photothermally-induced scattered field may contribute appreciably to the total signal as described by Eqs. 3 and 7. To investigate this size-dependent effect, we adopt an approximate core-shell polarizability model with a large nanoparticle core and a thermal lens of radius $r_{\rm th}$ representing the shell.²³

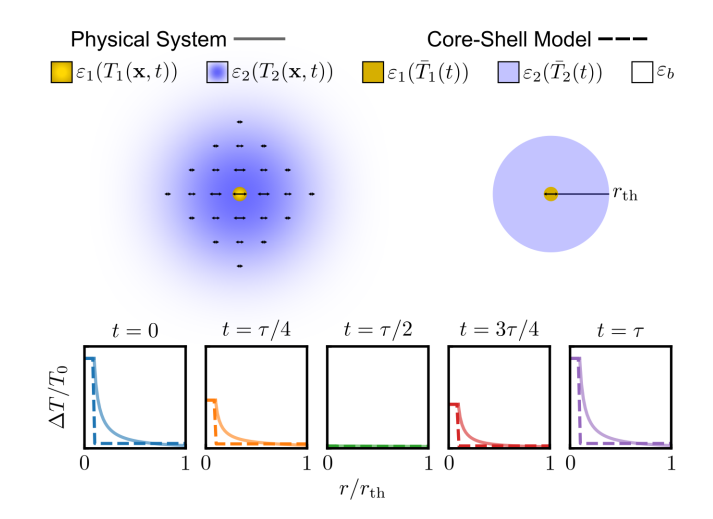


Figure 1: Schematic of a heated metal nanoparticle surrounded by a thermal lens (left) compared to the approximate core-shell polarizabilty model employed herein (right). The lower panels display a time series of the thermal profiles associated with each over one modulation period $\tau = 2\pi/\Omega$.

Specifically, the core-shell photothermal polarizability 24 is

$$\alpha_{\rm pt}(t) = \frac{1}{3} r_{\rm th}^3 \varepsilon_b \frac{(\varepsilon_2 - \varepsilon_b)[\varepsilon_1 q_1 - \varepsilon_2 (q_1 - 1)] r_{\rm th}^3 - (\varepsilon_1 - \varepsilon_2)[\varepsilon_2 (q_2 - 1) - \varepsilon_b q_2] a^3}{[\varepsilon_1 q_1 - \varepsilon_2 (q_1 - 1)][\varepsilon_2 q_2 - \varepsilon_b (q_2 - 1)] r_{\rm th}^3 - (\varepsilon_1 - \varepsilon_2)(\varepsilon_2 - \varepsilon_b) q_2 (q_2 - 1) a^3},$$
(14)

where $\varepsilon_1 \equiv \varepsilon_1(\bar{T}_1(t))$ is the dielectric function of the core at $\bar{T}_1(t)$, $\varepsilon_2 \equiv \varepsilon_2(\bar{T}_2(t))$ is the dielectric function of the background at $\bar{T}_2(t)$, and $q_i = 1/3 - (1/3)x_i^2 - i(2/9)x_i^3$ ($x_i = 2\pi r_i/\lambda_{\rm pu}$, $r_1 = a, r_2 = r_{\rm th}$) are the depolarization factors introduced to account for retardation effects. ^{24,25} In the small core radius limit ($x_1 = ka \ll 1$), Eq. 14 reduces to the ClausiusMossotti polarizability in Eq. 9. Figure 1 displays a schematic of the core-shell polarizability model and compares it to the true physical system in space (upper) and time (lower). A more

complete description of the latter would entail dividing the core and shell into multiple layers
to better characterize the full gradient profile of the thermal lens. Such an approach, however, while more accurate, would necessarily involve complicated numerical simulations and
would obscure the qualitative physical interpretation of the photothermal signal provided by
the core-shell model adopted.

Using the chain rule to calculate the derivatives of α_{pt} with respect to temperature, Eq. 8 now becomes

$$\alpha_{\rm pt}(t) \approx \alpha_{\rm pt}(T_0) + \sum_{j=1,2} \frac{\partial \alpha_{\rm pt}}{\partial n_j} \frac{\partial n_j}{\partial T} \Big|_{T_0} \bar{T}_j(t),$$
 (15)

where the average core and shell temperatures $\bar{T}_1(t) = T(|\mathbf{x}| = a, t)$ and $\bar{T}_2(t) = (4\pi/V_{\text{th}}) \int_a^{r_{\text{th}}} T(\mathbf{x}, t) r^2 dr$ are calculated according to a spherical absorber of radius a where

$$T(\mathbf{x},t) = \frac{P_{\text{pu}}}{8\pi\kappa r} \left[1 + \frac{e^{-(r-a)/r_{\text{th}}}}{((a+r_{\text{th}})/r_{\text{th}})^2 + (a/r_{\text{th}})^2} \left\{ \frac{a+r_{\text{th}}}{r_{\text{th}}} \cos\left(\Omega t - \frac{r-a}{r_{\text{th}}}\right) + \frac{a}{r_{\text{th}}} \sin\left(\Omega t - \frac{r-a}{r_{\text{th}}}\right) \right\} \right]$$
(16)

for $r \geq a$. By substituting these average core-shell temperatures into Eq. 15, the lock-in integration of Eq. 3 results in the generalized photothermal signal components

$$\Phi_{\text{int}\left\{\substack{\sin \\ \cos s}\right\}} = \frac{4k}{w_0^2 \sqrt{1 + (z_{\text{pr}}/z_R)^2}} \text{Im} \left[e^{i \tan^{-1}(-z_{\text{pr}}/z_R)} \frac{\Omega}{2\pi} \int_0^{2\pi/\Omega} \left(\sum_{j=1,2} \frac{\partial \alpha_{\text{pt}}}{\partial n_j} \frac{\partial n_j}{\partial T} \Big|_{T_0} \bar{T}_j(t) \right)^* \begin{Bmatrix} \sin \Omega t \\ \cos \Omega t \end{Bmatrix} dt \right]$$

$$= \frac{4k}{\sqrt{1 + (z_{\text{pr}}/z_R)^2}} \cdot \frac{\sigma_{\text{abs}}(\lambda_{\text{pu}})}{V_{\text{th}}\kappa} \cdot \frac{r_{\text{th}}^2}{w_0^2} \cdot \frac{2P_{\text{pu}}}{\pi w_{\text{pu}}^2}$$

$$\cdot \text{Im} \left[e^{i \tan^{-1}(-z_{\text{pr}}/z_R)} \sum_{j=1,2} \frac{\partial \alpha_{\text{pt}}^*}{\partial n_j} \frac{\partial n_j}{\partial T} \Big|_{T_0} \begin{Bmatrix} \mathcal{S}_j \\ \mathcal{C}_j \end{Bmatrix} \right] \tag{17}$$

$$\Phi_{\text{sca}\left\{\substack{\sin \\ \cos s}\right\}} = \frac{k^{4}}{z_{R}^{2} + z_{\text{pr}}^{2}} \frac{\Omega}{2\pi} \int_{0}^{2\pi/\Omega} \left| \alpha_{\text{pt}}(T_{0}) + \sum_{j=1,2} \frac{\partial \alpha_{\text{pt}}}{\partial n_{j}} \frac{\partial n_{j}}{\partial T} \right|_{T_{0}} \bar{T}_{j}(t) \right|^{2} \left\{\substack{\sin \Omega t \\ \cos \Omega t}\right\} dt$$

$$= \frac{k^{4}}{z_{R}^{2} + z_{\text{pr}}^{2}} \left(\frac{\sigma_{\text{abs}}(\lambda_{\text{pu}})r_{\text{th}}^{2}}{V_{\text{th}}\kappa} \cdot \frac{2P_{\text{pu}}}{\pi w_{\text{pu}}^{2}} \cdot 2\text{Re} \left[\alpha_{\text{pt}}(T_{0})^{*} \sum_{j=1,2} \frac{\partial \alpha_{\text{pt}}^{*}}{\partial n_{j}} \frac{\partial n_{j}}{\partial T} \right|_{T_{0}} \left\{\substack{S_{j} \\ C_{j}}\right\} \right]$$

$$+ \left(\frac{\sigma_{\text{abs}}(\lambda_{\text{pu}})r_{\text{th}}^{2}}{V_{\text{th}}\kappa} \cdot \frac{2P_{\text{pu}}}{\pi w_{\text{pu}}^{2}}\right)^{2} \cdot \left(\left|\frac{\partial \alpha_{\text{pt}}^{*}}{\partial n_{1}} \frac{\partial n_{1}}{\partial T}\right|_{T_{0}}\right)^{2} \cdot \left\{\substack{S_{q1} \\ C_{q1}}\right\} + 2\text{Re} \left[\frac{\partial \alpha_{\text{pt}}^{*}}{\partial n_{1}} \frac{\partial n_{1}}{\partial T} \frac{\partial \alpha_{\text{pt}}^{*}}{\partial n_{2}} \frac{\partial n_{2}}{\partial T}\right] \left\{\substack{S_{\text{int}} \\ C_{\text{int}}}\right\}$$

$$+ \left|\frac{\partial \alpha_{\text{pt}}^{*}}{\partial n_{2}} \frac{\partial n_{2}}{\partial T}\right|_{T_{0}}\right|^{2} \cdot \left\{\substack{S_{q2} \\ C_{q2}}\right\}\right)$$
(18)

evaluated along the optical axis with total signal $\Phi_{\text{cos}} = \Phi_{\text{int}\{\text{cos}\}} + \Phi_{\text{sca}\{\text{cin}\}}$ and

$$\alpha_{\rm pt}(T_0) = \frac{a^3}{3} \varepsilon_b \frac{\varepsilon_1(\omega) - \varepsilon_b}{\varepsilon_1(\omega) q_1 - \varepsilon_b(q_1 - 1)}
\frac{\partial \alpha_{\rm pt}}{\partial n_1} \Big|_{T_0} = \frac{2a^3}{3} \varepsilon_b^2 \frac{\sqrt{\varepsilon_1(\omega)}}{[\varepsilon_1(\omega) q_1 - \varepsilon_b(q_1 - 1)]^2}
\frac{\partial \alpha_{\rm pt}}{\partial n_2} \Big|_{T_0} = \frac{2\sqrt{\varepsilon_b}}{3} \Big[\frac{r_{\rm th}^6(\varepsilon_b(q_1 - 1) - \varepsilon_1 q_1)^2 + a^6(\varepsilon_1 - \varepsilon_b)^2(q_2 - 1)q_2}{r_{\rm th}^3[\varepsilon_b(q_1 - 1) - \varepsilon_1 q_1]^2}
+ \frac{a^3 r_{\rm th}^3[\varepsilon_1^2 q_1(1 - 2q_2) + \varepsilon_b^2(q_1 + 2q_2 - 2q_1 q_2 - 1) + 2\varepsilon_1 \varepsilon_b(2q_1 q_2 - q_1 - q_2)]}{r_{\rm th}^3[\varepsilon_b(q_1 - 1) - \varepsilon_1 q_1]^2} \Big],$$
(19)

where the \mathcal{S} , \mathcal{C} terms are defined in the Supporting Information.

Thus we find that introduction of a large nanoparticle core to the polarizability model 153 enhances the photothermally-induced scattering contribution $\Phi_{\rm sca{sin}\atop cos}$ to the signal that 154 carries a nonlinear dependence upon the pump power P_{pu} . Certainly this term is suppressed 155 by a factor proportional to the square of the thermo-optic coefficients of the core and shell, 156 but it is also enhanced by the resonant responses of the nanoparticle core encoded in the 157 absorption cross section $\sigma_{\rm abs}$ as well as through the resonances of $\partial \alpha_{\rm pt}/\partial n_1$ and $\partial \alpha_{\rm pt}/\partial n_2$ at 158 the pump wavelength in Eq. 19. These resonances of $\sigma_{\rm abs}$ and $d\alpha_{\rm pt}/dT$ provide additional 159 enhancements of this scattering-like photothermal signal contribution beyond its quadratic pump power dependence. Said differently, the importance of $\Phi_{\text{sca}\left\{\substack{\sin \\ \cos s}\right\}}$ depends critically upon the properties of the core polarizability, which can be influenced by nanoparticle size and 162 composition as well as through resonance effects that are all well understood for plasmonic systems. In the small particle limit ($ka \ll 1$), $\Phi_{\rm int}$ in Eq. 17 reduces to that of Eq. 12 and $\Phi_{\rm sca}$ in Eq. 18 becomes negligible at low pump powers. Note that the small particle limit can be achieved equivalently by either decreasing the nanoparticle size at fixed probe wavelength or by increasing the probe wavelength at fixed nanoparticle size. Also, note that resonant scattering of the probe would be filtered out by lock-in detection and thus would not contribute to the photothermal signal Φ .

$_{\scriptscriptstyle{70}}$ Photothermal Spectra

189

As reported in the literature¹ and shown explicitly in Eq. 12 above, the photothermal signal is a measure of absorption in the thermal lensing limit appropriate for small absorbing
nano-objects. However, for larger particles, such as for plasmonic nanoparticle antennas,
non-negligible scattering contributions arise and call into question some of the approximations made in the thermal lensing limit. Those approximations can change the resulting
interpretation.

Through numerical solution of Eqs. 17–18, we now investigate the evolution of the 177 photothermal signal when these consequences begin to take effect for gold nanospheres of 178 varying radius (a = 10, 20, 100 nm) embedded in a glycerol medium. Fig. 2 shows pump 179 wavelength-dependent photothermal spectra calculated with a fixed probe wavelength of 785 180 nm as a function of pump power. In each panel, the black trace is the photothermal signal 181 $|\Phi|$ post lock-in detection together with the sine and cosine parts of its interference (blue 182 trace) and scattering (red trace) components, while the underlying gray and purple shaded 183 spectra correspond to Mie absorption and scattering cross sections ($\sigma_{abs,sca}$), including terms 184 up to $\ell = 10$. The scattering cross section for a = 100 nm is reduced by a factor of two to 185 display all traces within the same viewing window. In addition, the photothermal signal and 186 its components are scaled by the area $\pi w_{\rm pu}^2/2$ of the pump beam waist, as was done in our prior experiment. 11 188

The upper, middle, and lower rows of Fig. 2a correspond to pump powers of 100, 200, and

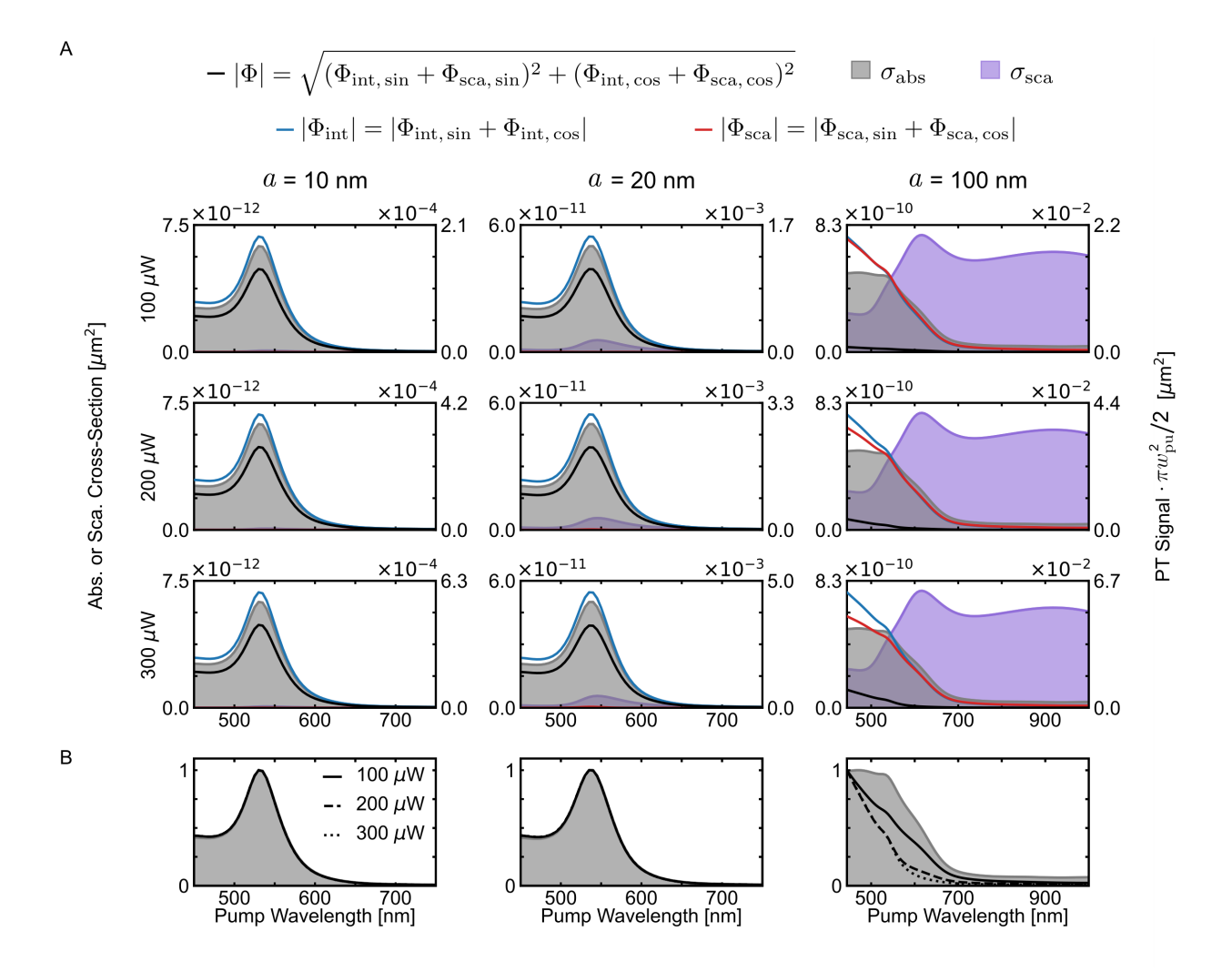


Figure 2: Photothermal spectra of the core-shell model with retardation of gold nanospheres of radius 10 nm, 20 nm, and 100 nm. The photothermal signal $|\Phi|$ is evaluated in the far-field on the optical axis ($\theta=0^{\circ}$, $\phi=0^{\circ}$) and is scaled by the pump beam waist area. (A) The gray and purple shaded regions are the $\ell=10$ Mie absorption and scattering cross sections, respectively. The Mie scattering cross section for a=100 nm has been reduced by a factor of two to fit within each panel. The black trace is the total photothermal signal, while the blue and red traces are the sum of the sine and cosine parts of $|\Phi_{\rm int}|$ and $|\Phi_{\rm sca}|$, respectively. In all panels, the heating beam wavelength is varied while the probe beam wavelength is fixed at 785 nm. The beam waists at the focus of the pump and probe lasers are taken to be diffraction limited at each wavelength. Specific pump and probe wavelengths, beam waists, and focal positions $z_{\rm pu}$ (0 – 1 μ m) and $z_{\rm pr}$ (0.9 μ m) are chosen to be consistent with experiment (see below). (B) Replot of data from (A) with normalized Mie absorption (shaded gray) overlaid against the normalized total photothermal signals at the three different powers chosen to model the experimental conditions described below.

 $300 \,\mu\mathrm{W}$, respectively, using a pump beam waist ranging from 216 nm to 456 nm depending on the pump wavelength. For the a = 10 and 20 nm nanoparticles the interference contribution 191 (blue) dominates the signal and Φ closely tracks the absorption cross section (black lineshape 192 compared to shaded gray lineshape) as can be seen most clearly in Fig. 2b. These numerical 193 results indicate that photothermal imaging may be used as a proxy for an absorption cross 194 section measurement for small particles at these pump powers, an understanding that has 195 been well established in the literature for lower pump powers. ⁶ For the a=100 nm nanopar-196 ticle, both interference (blue) and scattering (red) contributions contribute nearly equally to 197 the signal, and the photothermal spectrum only approximately tracks the absorption cross 198 section lineshape, with deviations occurring at longer wavelengths. However, as the pump 199 power decreases, the photothermal spectrum of the 100 nm radius particles approaches the 200 lineshape of the absorption cross section. 201

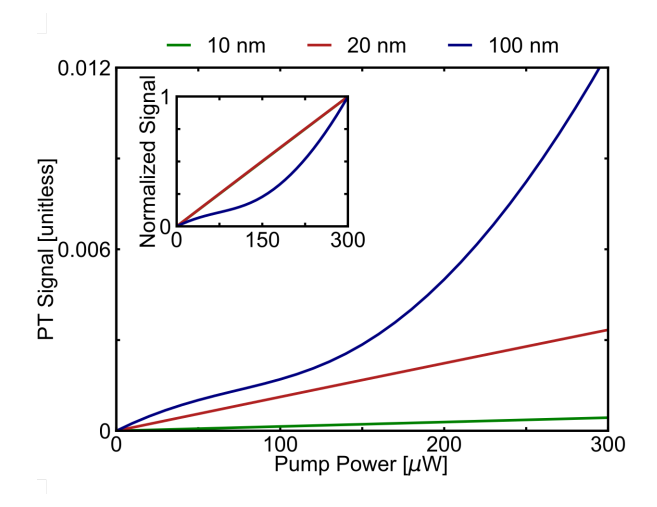


Figure 3: Photothermal signal as a function of pump laser power at a fixed pump (532 nm) and probe (785 nm) wavelength for 10 nm (green), 20 nm (red), and 100 nm (blue) radius gold nanospheres. The relationship between the pump laser power and the photothermal signal is approximately linear for the 10 nm and 20 nm radius nanospheres. However, for larger particles, the dependency of the signal on the pump power becomes nonlinear. The inset shows the photothermal signals normalized to the highest pump power.

To further investigate the pump power dependence demonstrated in Fig. 2, Fig. 3 displays the evolution of the photothermal signal with varying pump power for the a = 10, 20, and 100 nm gold nanoparticles described previously. The pump laser wavelength is fixed

at 532 nm and the probe laser wavelength is 785 nm. For 10 nm (green trace) and 20 nm (red trace) particles, the photothermal signal depends approximately linearly upon pump 206 power. However, for the 100 nm particles (blue trace) a pronounced nonlinearity in pump 207 power dependence is clearly evident. This nonlinear behavior exhibited in the second term 208 of the scattering-like contribution $\Phi_{\text{sca}\left\{\substack{\sin \\ \cos \right\}}}$ in Eq. 18 and calculated in Fig. 3 for realistic 209 experimental parameters (see below) is surprising, given the quadratic dependence upon the 210 small ($\sim 10^{-4}~{\rm K}^{-1}$) thermo-optic coefficients of the nanoparticle and surrounding medium. 211 However, this quadratic dependence clearly becomes relevant in the photothermal response 212 of large particles at higher pump powers. 213

214 Experiment

To test the predictions of our theoretical model of photothermal imaging and spectroscopy, 215 we imaged samples of gold nanoparticles with nominal radii of 10, 20, and 100 nm with our 216 confocal, photothermal microscope. Fig. 4 summarizes their optical extinction and size dis-217 tribution. The nanoparticle samples were spincast onto separate glass coverslips. Adhesive 218 rubber spacers were used to make wells, which were filled with glycerol and sealed by placing 219 an additional glass coverslip on top forming a glass-gold nanoparticle-glycerol-glass sandwich. The samples were imaged on our photothermal microscope described previously. 10,11 Briefly, the intensity modulated 532 nm pump and unmodulated 785 nm probe lasers (Coherent, 222 Obis) were colinearly focused onto the sample using a $63 \times /1.4$ numerical aperture (NA) objective (Zeiss, Plan-Apochromat). The pump and probe beam diameters are 260 and 224 650 nm at full width at half maximum (FWHM), respectively, measured via a knife edge 225 method. The transmitted probe beam was collected with a $40 \times /0.6$ NA objective (Zeiss, 226 Plan-Neofluoar) and focused onto a Si photodiode (FEMTO, HCA-S 200M-Si) and the pho-227 tothermally modulated signal was detected with a lock-in amplifier (SRS, SR844) at the 228 pump beam modulation frequency of 100 kHz.

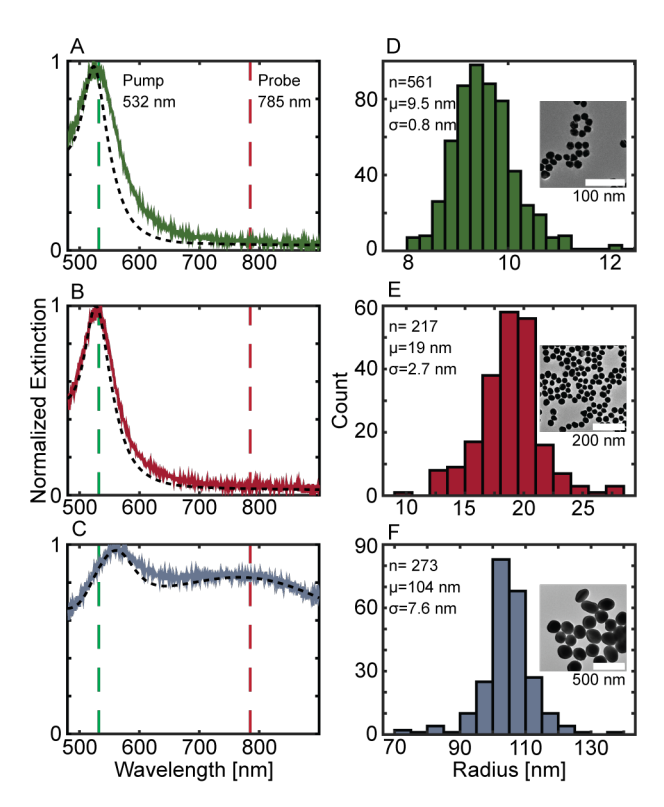


Figure 4: Ensemble extinction spectra of (A) 10, (B) 20, and (C) 100 nm radius gold nanoparticles in water. Solid lines indicate experimental spectra and dashed lines indicate the corresponding theoretical Mie theory extinction spectra in a 1.33 refractive index medium. Dashed green and red lines correspond to the pump and probe wavelengths of 532 and 785 nm, respectively. Particle size distributions of (D) 10, (E) 20, and (F) 100 nm radius gold nanoparticles. Insets: representative transmission electron microscopy images. The distributions are presented in panels D–F with the numbers of particles, and particle size means and standard deviations indicated.

Photothermal images of the 10, 20, and 100 nm radius gold nanoparticles were obtained 230 by using a nanopositioning piezo stage (Physik Instrumente, PI-517.2CL) to scan the sample 231 through the focus of the pump and probe laser beams generating a photothermal image of the 232 gold nanoparticles as demonstrated in Fig. 5A-C. The photothermal intensity is measured 233 as the ratio of the maximum lock-in amplitude of each particle to the probe power measured 234 before the microscope with units of mV/mW. We use this definition of photothermal intensity 235 for the experiments, normalizing to the probe power, because the probe power had to be 236 changed between the different particle sizes to keep the modulated signal within the operating 237 limits of the lock-in amplifier. To ensure that these different probe powers did not introduce 238 any unexpected behavior, we confirmed that the probe power dependence is linear for all 230 probe powers tested (Fig. S1), as is expected from previous literature⁵ and theory. Fig. 240 5D shows that the photothermal intensity is clearly size dependent with the 20 nm radius 241 gold nanoparticles having a maximum signal that is approximately 8× that of the 10 nm 242 radius gold nanoparticles at the same pump power. This change in photothermal intensity 243 is consistent with previous experimental results^{3,4} as well as the theory of the generalized 244 photothermal signal presented above where photothermal signal scales with the cube of the 245 nanoparticle radius in the small particle limit, Eq. 12. However, the photothermal intensity increases by only 3.6× (Fig. 5D) when increasing the size from 20 nm to 100 nm radius for a similar pump power due to additional resonance effects of the 100 nm radius gold nanoparticle at the probe wavelength of 785 nm (Fig. 4C), similar to the effect seen in Fig. 249 2 when comparing the photothermal signal of different gold nanoparticle sizes at a constant 250 pump power and wavelength. 251

We further investigated the size and pump power dependence of the photothermal signal by recording photothermal images of the 10, 20, and 100 nm radius gold nanoparticles under various pump powers between 20 and 310 μ W measured at the sample plane (50 – 750 kW· cm⁻²). To ensure that the observed trends were robust and that there was no photothermal damage to our nanoparticles under the highest pump powers, we varied the pump powers

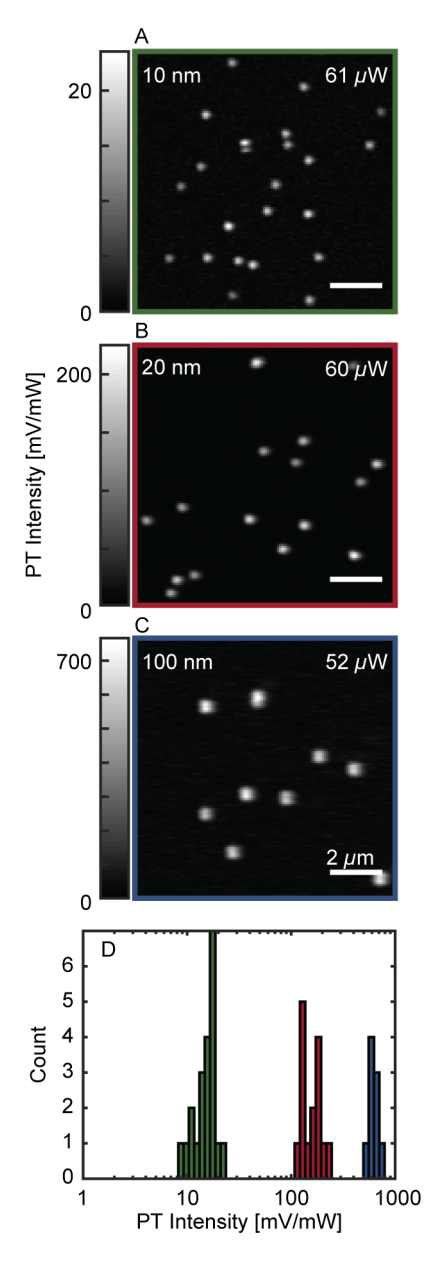


Figure 5: Single particle photothermal images of (A) 10, (B) 20, and (C) 100 nm radius gold nanoparticles under similar pump powers. Scale bars are 2 μ m. Note the differences in photothermal intensities and PSF spot sizes. (D) Intensity distributions for the particles shown in A–C. The green, red, and blue histograms are the 10, 20, and 100 nm radius gold nanoparticles, respectively.

in random order and repeated each measurement three times. We further verified that no damage occurred by comparing correlated SEM images of 100 nm radius gold nanoparticles that were either exposed or unexposed to our highest pump power of 310 μ W. The size distributions are shown in Fig. S2 and a one-way analysis of variance revealed that there was not a statistically significant difference between the exposed and unexposed particle sizes (F(1, 266) = 0.25, p = 0.62).

We first compare the effect of the pump power on the size of the image point spread 263 function (PSF), Fig. 6. We fit the photothermal PSFs with 2D Gaussians to determine the 264 FWHM of the gold nanoparticles as a function of pump power. Example linesections and 265 single particle images are presented in Fig. 6A–F for low power (60 μ W, 150 kW \cdot cm⁻²) and 266 high power (210 μW , 525 kW · cm⁻²) excitations. The entire power range is summarized 267 in Fig. 6G. At low power, as the particle increases in size, the FWHM increases due to a 268 convolution of the gold nanoparticle size and the pump beam width (260 nm FWHM). This 269 effect accounts for a broadening of ~ 3 and 70 nm for the 20 and 100 nm radius nanoparticles, 270 respectively. Additional broadening of the PSF could be due to changes in the probe beam 271 focus position, which was changed commensurately with the pump beam to maximize the 272 intensity of the photothermal signal for each particle size. For the 10 and 20 nm radius gold nanoparticles, we observe a power independent photothermal PSF FWHM (Fig. 6A–D, G), consistent with theoretical analysis in the small particle limit, Eqs. 12 and S8. However, in 275 the large particle limit, the photothermal PSF has contributions from both the Φ_{int} and Φ_{sca} 276 terms leading to a narrowing of the photothermal PSF at higher pump powers (Fig. 6F, G) 277 as described by Eqs. 17 and S2. Note, the intensity spike in the PSF in Fig. 6F is random; 278 some particles exhibit a spike, while some do not. 279

We next compare the effect of the pump power on the photothermal intensities for the gold nanoparticles extracted from the photothermal images, Fig. 7. The photothermal intensity is defined the same way as in Fig. 5. For the small 10 and 20 nm radius gold nanoparticles we observe the expected linear pump power relationship as described in the

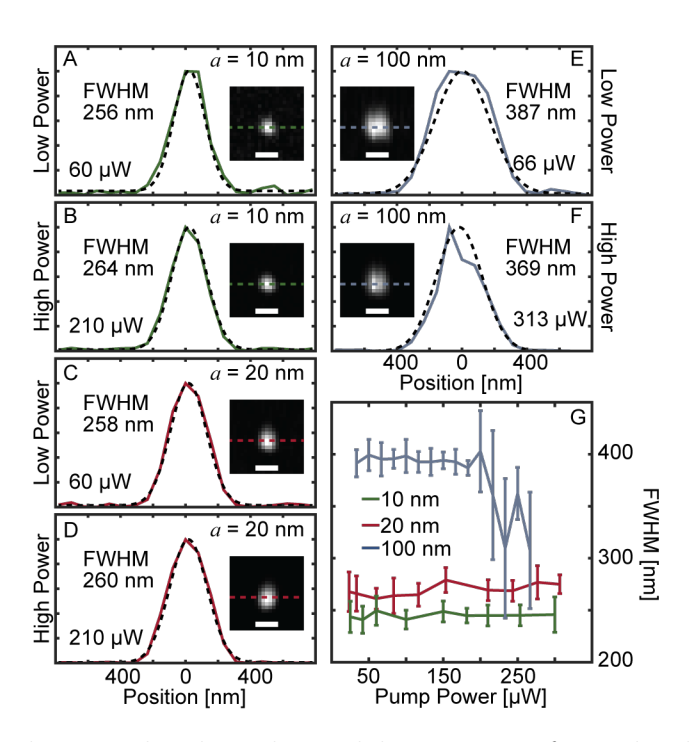


Figure 6: (A–F) Single particle photothermal linesections for individual 10, 20, and 100 nm gold nanoparticles under low (150 kW \cdot cm⁻²) and high (525 kW \cdot cm⁻²) pump powers. Dashed lines are Gaussian fits. Insets: PSFs of single particles correspond to the linesections. Scale bars are 500 nm. (G) Mean FWHM as a function of pump power for each of the nanoparticle size distributions. Error bars are standard deviation from multiple particles within each image and with three repeat measurements.

small particle limit where $\Phi_{\rm int}$ is linearly-dependent on $P_{\rm pu}$ and $\Phi_{\rm sca} \ll \Phi_{\rm int}$. However, for the large 100 nm radius gold nanoparticles, we observe a linear plus quadratic pump 285 power dependence due to the $P_{\rm pu}^2$ term in $\Phi_{\rm sca}$. While the magnitudes of the pump power 286 dependencies are different between theory and experiment, possibly due to the influence of 287 the substrate in the experiment which is not modeled in the analytical theory, the qualitative 288 trends remain. We note that this nonlinear trend could also be observed by locking into 2Ω 289 modulation to directly measure the quadratic term in $\Phi_{\rm sca}$, though that is not done in this 290 work. Thus, the major trends expected from the generalized photothermal theory presented 291 above are experimentally supported. 292

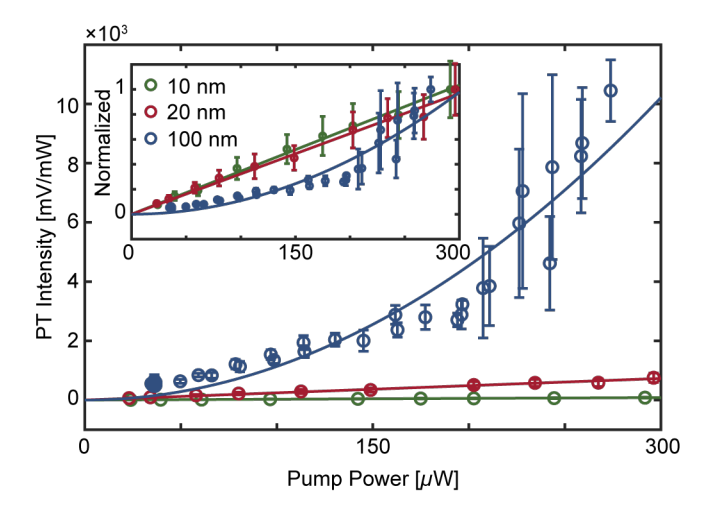


Figure 7: Pump power dependence of the 10 (green), 20 (red), and 100 (blue) nm radius gold nanoparticles. The solid lines are fits to the data. Inset: normalized to the highest pump power.

93 Conclusion

In this article, we assess the scattering effects of large nanoparticles upon the confocal photothermal experiment using an effective dipole model and companion photothermal spectroscopy and imaging experiments of individual plasmonic gold nanoparticles. For small nanoparticles ($ka \ll 1$), the pump wavelength-resolved photothermal signal is directly proportional to the absorption cross section, as is well understood in the literature. However for

larger nanoparticles $(ka \sim 1)$, we find the photothermal spectrum to deviate from the absorption spectrum through the addition of a new scattering term $\Phi_{\rm sca}$ that depends nonlinearly 300 upon the pump intensity. While $\Phi_{\rm sca}$ resembles the scattering cross section $\sigma_{\rm sca}$ of a dipole, 301 i.e., both carry the same k^4 and $|\alpha|^2$ dependence, the two signals are distinctly different 302 in their underlying polarizabilities: $\Phi_{\rm sca}$ is proportional to the photothermal polarizability 303 $\alpha_{\rm pt}(t) = \alpha(T_0) + (d\alpha_{\rm pt}/dn)(dn/dT)\Big|_{T_0} \bar{T}(t)$, while $\sigma_{\rm sca}$ depends upon the Mie polarizability 304 $\alpha(T_0)$. As a result of this photothermal scattering term, the photothermal spectrum of larger 305 nanoparticles at higher pump intensities is no longer directly proportional to the absorption 306 cross section. These predictions, which distinguish small and large nanoparticle limits, are 307 evaluated by companion experiments of pump laser power-dependent photothermal images 308 of spherical gold nanoparticles from $\sim 10-100$ nm in radius and $\sim 20-300~\mu\mathrm{W}$ in pump 309 power $(50 - 750 \text{ kW} \cdot \text{cm}^{-2})$, where the nonlinearity begins to dominate at pump intensities 310 in excess of 500 kW \cdot cm⁻² for the \sim 100 nm radius particles. Excellent agreement between 311 experiment and prediction is shown, highlighting the importance of photothermally induced 312 scattering upon the interpretation of the photothermal signal from larger nanoparticles at 313 higher pump intensities. 314

315 Acknowledgments

This work was supported by the U.S. National Science Foundation under Grants CHE-1727092 and CHE-2118333 (D.J.M), CHE-1727122 and CHE-2118420 (S.L.), and CHE-1728340 and CHE-2118389 (K.A.W.). S.L. also acknowledges support from the Charles W. Duncan, Jr.-Welch Chair in Chemistry (C-0002). The experimental work was conducted in part using resources of the Shared Equipment Authority at Rice University.

321 Data Availability

The data that support the findings of this study are available from the corresponding authors upon reasonable request.

References

- (1) Adhikari, S.; Spaeth, P.; Kar, A.; Baaske, M. D.; Khatua, S.; Orrit, M. Photothermal
 microscopy: imaging the optical absorption of single nanoparticles and single molecules.
 ACS Nano 2020, 14, 16414–16445.
- Vermeulen, P.; Cognet, L.; Lounis, B. Photothermal microscopy: optical detection of small absorbers in scattering environments. J. Microsc. **2014**, 254, 115–121.
- 330 (3) Boyer, D.; Tamarat, P.; Maali, A.; Lounis, B.; Orrit, M. Photothermal imaging of 331 nanometer-sized metal particles among scatterers. *Science* **2002**, *297*, 1160–1163.
- (4) Berciaud, S.; Cognet, L.; Blab, G. A.; Lounis, B. Photothermal heterodyne imaging
 of individual nonfluorescent nanoclusters and nanocrystals. *Phys. Rev. Lett.* **2004**, *93*,
 257402.
- (5) Gaiduk, A.; Ruijgrok, P. V.; Yorulmaz, M.; Orrit, M. Detection limits in photothermal
 microscopy. Chem. Sci. 2010, 1, 343–350.
- (6) Huang, Y.-C.; Chen, T.-H.; Juo, J.-Y.; Chu, S.-W.; Hsieh, C.-L. Quantitative imaging of single light-absorbing nanoparticles by widefield interferometric photothermal
 microscopy. ACS Photonics 2021, 8, 592–602.
- ³⁴⁰ (7) Zeng, Z.-C.; Wang, H.; Johns, P.; Hartland, G. V.; Schultz, Z. D. Photothermal mi-³⁴¹ croscopy of coupled nanostructures and the impact of nanoscale heating in surface-³⁴² enhanced raman spectroscopy. *J. Phys. Chem. C* **2017**, *121*, 11623–11631.

- ³⁴³ (8) Knapper, K. A.; Pan, F.; Rea, M. T.; Horak, E. H.; Rogers, J. D.; Goldsmith, R. H. Single-particle photothermal imaging via inverted excitation through high-Q all-glass toroidal microresonators. *Opt. Express* **2018**, *26*, 25020–25030.
- 9) Bhattacharjee, U.; West, C. A.; Hosseini Jebeli, S. A.; Goldwyn, H. J.; Kong, X.-T.; Hu, Z.; Beutler, E. K.; Chang, W.-S.; Willets, K. A.; Link, S., et al. Active far-field control of the thermal near-field via plasmon hybridization. *ACS Nano* **2019**, *13*, 9655–9663.
- (10) Hosseini Jebeli, S. A.; West, C. A.; Lee, S. A.; Goldwyn, H. J.; Bilchak, C. R.;
 Fakhraai, Z.; Willets, K. A.; Link, S.; Masiello, D. J. Wavelength-Dependent Photothermal Imaging Probes Nanoscale Temperature Differences among Subdiffraction
 Coupled Plasmonic Nanorods. Nano Lett. 2021,
- Yorulmaz, M.; Nizzero, S.; Hoggard, A.; Wang, L.-Y.; Cai, Y.-Y.; Su, M.-N.; Chang, W. S.; Link, S. Single-particle absorption spectroscopy by photothermal contrast. *Nano Lett.* 2015, 15, 3041–3047.
- (12) Heylman, K. D.; Thakkar, N.; Horak, E. H.; Quillin, S. C.; Cherqui, C.; Knapper, K. A.;
 Masiello, D. J.; Goldsmith, R. H. Optical microresonators as single-particle absorption
 spectrometers. *Nature Photonics* 2016, 10, 788–795.
- Thakkar, N.; Rea, M. T.; Smith, K. C.; Heylman, K. D.; Quillin, S. C.; Knapper, K. A.;
 Horak, E. H.; Masiello, D. J.; Goldsmith, R. H. Sculpting Fano Resonances To Control
 Photonic-Plasmonic Hybridization. Nano Letters 2017, 17, 6927–6934.
- ³⁶³ (14) Pan, F.; Smith, K. C.; Nguyen, H. L.; Knapper, K. A.; Masiello, D. J.; Goldsmith, R. H. Elucidating Energy Pathways through Simultaneous Measurement of Absorption and Transmission in a Coupled Plasmonic–Photonic Cavity. *Nano Letters* **2020**, *20*, 50–58.
- 366 (15) Shi, Z.; Huang, J.; Huang, X.; Huang, Y.; Wu, L.; Li, Q. Resonant scattering enhanced 367 interferometric scattering microscopy. *Nanoscale* **2020**, *12*, 7969–7975.

- ³⁶⁸ (16) Taylor, R. W.; Sandoghdar, V. Interferometric scattering microscopy: seeing single nanoparticles and molecules via Rayleigh scattering. *Nano Lett.* **2019**, *19*, 4827–4835.
- Young, G.; Kukura, P. Interferometric scattering microscopy. *Annu. Rev. Phys. Chem.* **2019**, 70, 301–322.
- (18) Paulo, P. M.; Gaiduk, A.; Kulzer, F.; Krens, S. G.; Spaink, H. P.; Schmidt, T.; Orrit, M.
 Photothermal correlation spectroscopy of gold nanoparticles in solution. J. Phys. Chem.
 C 2009, 113, 11451–11457.
- ³⁷⁵ (19) Selmke, M.; Cichos, F. The physics of the photothermal detection of single absorbing nano-objects: A review. *arXiv preprint arXiv:1510.08669* **2015**,
- 377 (20) Goldwyn, H. J.; Link, S.; Masiello, D. J. Resolving resonance effects in the theory of 378 single particle photothermal imaging. arXiv preprint arXiv:2103.01494 2021,
- 379 (21) Brown, B. S.; Hartland, G. V. Influence of Thermal Diffusion on the Spatial Resolution 380 in Photothermal Microscopy. *The Journal of Physical Chemistry C* **2022**, *126*, 3560– 381 3568.
- ³⁸² (22) Selmke, M.; Braun, M.; Cichos, F. Gaussian beam photothermal single particle mi-³⁸³ croscopy. J. Opt. Soc. Am. A **2012**, 29, 2237–2241.
- Baaske, M. D.; Asgari, N.; Spaeth, P.; Adhikari, S.; Punj, D.; Orrit, M. Photothermal
 Spectro-Microscopy as Benchmark for Optoplasmonic Bio-Detection Assays. J. Phys.
 Chem. C 2021, 125, 25087–25093.
- ³⁸⁷ (24) Chung, H.-Y.; Leung, P.-T.; Tsai, D.-P. Dynamic modifications of polarizability for large metallic spheroidal nanoshells. *J. Chem. Phys.* **2009**, *131*, 124122.
- ³⁸⁹ (25) Moroz, A. Depolarization field of spheroidal particles. J. Opt. Soc. of Am. B **2009**, 26, ³⁹⁰ 517–527.